Chinese Chemical Letters 37 (2026) 111227

Contents lists available at ScienceDirect

Chinese Chemical Letters

journal homepage: www.elsevier.com/locate/cclet

Strain-driven intermetallic PtCo nanozymes for high and specific peroxidase-like activity

Bo Xu [a,1], Mingjin Cui [a,b,1,*], Zhimin Luo [a,*], Lianhui Wang [a,*]

[a] State Key Laboratory of Organic Electronics and Information Displays (SKLOEID) & Jiangsu Key Laboratory for Biosensors, Institute of Advanced Materials (IAM), School of Chemistry and Life Sciences, College of Electronic and Optical Engineering & College of Flexible Electronics (Future Technology), Nanjing University of Posts and Telecommunications, Nanjing 210023, China

[b] Institute of Energy Materials Science (IEMS), University of Shanghai for Science and Technology, Shanghai 200093, China

ARTICLE INFO

Article history:
Received 17 March 2025
Revised 9 April 2025
Accepted 16 April 2025
Available online 17 April 2025

Keywords:
Pt-based intermetallic
Nanozymes
Core-shell structure
Strain regulation
Enzyme-like catalysis

ABSTRACT

Although the distinctive physicochemical properties of Pt-based intermetallic nanomaterials are well-recognized, the critical influence of Pt skin-induced lattice strain effects on their enzyme-mimicking catalytic performance remains unexplored. This knowledge gap primarily stems from the technical challenges in achieving atomic-level precision and structural uniformity when engineering active sites within Pt-based intermetallic systems. Herein, we demonstrate exceptional peroxidase-like catalytic activity (25.545 U/mg) and remarkable specificity through strain-engineered $L1_0$ PtCo@Pt core-shell architectures. Experimental and theoretical analyses reveal that significantly reduces H_2O_2 adsorption energy (-1.49 eV) and the energy barrier of rate-determining step (0.128 eV). This strain-driven electronic modulation enables a 17.4-fold enhancement in peroxidase-like activity compared to conventional Pt nanoparticles, establishing a quantitative correlation between interfacial lattice compression (3.5 % strain) and catalytic efficiency. Three key advances emerge from this work: (1) Identification of lattice strain as a dominant descriptor for nanozyme specificity in H_2O_2 activation, (2) development of a universal synthesis framework (<1 min) for ordered intermetallic core-shell systems, and (3) demonstration of strain engineering as a generalizable strategy exceeding noble metal-dependent activity enhancement. The developed methodology not only resolves long-standing challenges in scalable nanozyme production but also opens new avenues for designing biocatalysts through atomic-level strain manipulation.

© 2026 Published by Elsevier B.V. on behalf of Chinese Chemical Society and Institute of Materia Medica, Chinese Academy of Medical Sciences.

Nanozymes are defined as assemblies of nanomaterial-based artificial enzyme mimetics [1–6]. Due to their exceptional environmental tolerance, recyclability, and long-term stability, nanozymes are emerging as viable alternatives to natural enzymes [7–11]. These assemblies can consist of single or multi-component nanoscale noble metals, alloys, carbon materials, and other catalysts, and find wide applications in therapy and biosensing [12,13]. At the microstructural level, the flexibility in selecting active sites and the diversity in binding types and modes allow significant modifiability across multiple structural domains, offering immense potential. Noble metal nanozymes (*e.g.*, Pt) are particularly notable for their highly surface-functionalized properties, excellent biocompatibility, tunable physicochemical characteristics, and exceptional intrinsic enzyme-like activities, making them promising candidates for applications in biosensing, therapeutic, and antioxidant fields [14–18]. Despite significant progress, unclear catalytic mechanisms and poor selectivity remain bottlenecks in the development of noble metal nanozymes [19–22].

Conventional synthesis methods for noble metal nanozymes, such as hydrothermal and sol-gel approaches, often suffer from prolonged reaction times (hours to days) and inhomogeneous active site distributions, which hinder precise control over lattice strain and surface electronic states [23]. While strain engineering has emerged as a promising strategy to optimize catalytic performance in electrocatalysis [24], its application in nanozyme design faces two critical challenges: (1) Existing wet-chemical methods struggle to achieve uniform lattice strain at the core-shell interface, and (2) the structure-activity relationship between strain effects and enzyme-like specificity remains poorly understood. These limitations underscore the urgent need for innovative synthesis platforms capable of atomic-level strain modulation.

Numerous studies indicate that electrocatalyst design methods, such as those based on strain, ligand, electronic, and carrier effects,

* Corresponding authors.
E-mail addresses: mjcui@usst.edu.cn (M. Cui), iamzmluo@njupt.edu.cn (Z. Luo), iamlhwang@njupt.edu.cn (L. Wang).
[1] These authors contributed equally to this work.

https://doi.org/10.1016/j.cclet.2025.111227
1001-8417/© 2026 Published by Elsevier B.V. on behalf of Chinese Chemical Society and Institute of Materia Medica, Chinese Academy of Medical Sciences.

are currently a research focus. Among these, strain engineering to regulate catalyst electronic structures for optimizing catalytic performance has proven effective [25–28]. However, advancements are primarily limited by the complexities in achieving precise synthesis and uniform control of active sites within strain-effect nanomaterials.

Recent advances in intermetallic compounds (*e.g.*, $L1_0$-FePt) have demonstrated their exceptional stability and ordered atomic arrangements for oxygen reduction reactions [29]. However, their potential in biocatalysis, particularly in mimicking natural enzymes with high specificity, remains largely unexplored. A key unresolved question is whether the rigid atomic ordering of intermetallic compounds can synergize with surface strain engineering to lower the activation energy barriers in peroxide decomposition, a process critical for peroxidase-like activity.

Furthermore, the ordered structure of intermetallic compounds, characterized by strict stoichiometric requirements and favorable atomic bonding environments, endows them with unique electronic structures and surface adsorption sites [30–33]. Compared to disordered alloy catalysts, intermetallic compounds often exhibit superior peroxidase (POD)-like catalytic activity and structural stability [31,34]. Therefore, enhancing catalytic performance through strain-controlled surface engineering and intermetallic compound strategies, which increase surface strain and enhance catalyst activity and stability, represents an effective approach. While strain-controlled intermetallic compound catalysts have found widespread application in electrocatalysis, their potential in designing highly active and specific nanozymes for biocatalysis remains to be fully explored.

The synthesis of strain-engineered intermetallic nanozymes demands a technology that combines ultrafast kinetics with precise energy input. Here, Joule heating—a rapid thermal processing technique utilizing high-current pulses (typically <1 s), offers distinct advantages over conventional methods: (1) It suppresses nanoparticle agglomeration by minimizing high-temperature exposure, thereby preserving core-shell structural uniformity [35,36]; (2) enables sub-angstrom control of lattice strain through programmable current parameters ($\pm0.5\%$ error); and (3) facilitates atomic ordering in multi-metallic systems without phase segregation [37,38]. Compared to microwave-assisted synthesis, joule heating reduces energy consumption by $\sim60\%$ while maintaining scalability [39]. Nevertheless, its reliance on conductive substrates (*e.g.*, carbon frameworks) for homogeneous heating adds complexity to precursor design, and the millisecond-scale reaction kinetics pose challenges for *in situ* characterization of strain evolution.

Herein, we revolutionize Pt-based nanozyme development through an innovative $L1_0$ PtCo@Pt core-shell structure that synergizes the robustness of a PtCo intermetallic core with the catalytic prowess of a Pt-skin shell. Leveraging the aforementioned advantages of Joule heating, we successfully synthesized bimetallic core-shell PtCo@Pt nanozymes in a single step. This architecture exploits strain-induced effects at the core-shell interface to lower activation energy barriers, achieving a specific POD-like activity of 25.545 U/mg—17.4-fold higher than Pt nanoparticles—with negligible oxidase activities. Both experimental and theoretical analyses confirm that the Pt skin and interfacial strain collectively reduce H_2O_2 adsorption energy and rate-determining step barriers. Our rapid synthesis method pioneers a novel approach for nanozymes with exceptional activity and specificity, paving the way for biomedical advancements.

In this study, we designed core-shell structured PtCo intermetallic nanoparticles (iNPs) featuring a thin Pt skin as the active catalytic layer, which demonstrated high POD-like activity. The thermodynamically stable PtCo intermetallic core provides robustness and durability for catalytic applications. As illustrated in Fig. 1a, the $L1_0$ PtCo@Pt core-shell nanoparticles with an *in-situ* Pt shell were synthesized in a single step using a high-temperature shock method. Carbon black was employed as the substrate for synthesizing and loading the nanozymes due to its excellent conductivity and increased defect sites after CO_2 etching (details in Supporting information), which enhanced the anchoring and loading capacity for nanoparticles. The precursors, hydrogen hexachloroplatinate(IV) hydrate and cobalt(II) chloride hexahydrate, with a molar ratio of Pt/Co = 1.5, were loaded onto the carbon black powder. By rapidly heating (10^5 K/s) to high temperatures ($\sim$2000 K), PtCo nanoparticles were quickly synthesized, followed by a 1-min incubation. Subsequently, Pt and Co atoms formed an $L1_0$ face-centered tetragonal crystal system, producing the desired PtCo@Pt core-shell nanoparticles. Additionally, the excess Pt (molar ratio of Pt/Co = 1.5) tended to form an *in-situ* thin Pt shell on the PtCo intermetallic surface due to their lower surface energy (Pt surface energy = 1.48 eV/atom *vs.* Co surface energy = 2.04 eV/atom) [40]. This process enhanced the surface stability of the core-shell structure, and the subsequent rapid cooling effectively stabilized the final core-ordered PtCo structure with a Pt-enriched shell.

By adjusting the Joule heating process, we obtained PtCo structures with varying compositions and successfully synthesized homogeneously dispersed PtCo and Pt control groups. Pt nanozymes were synthesized using a similar process, except with only the Pt precursor and a 200 ms Joule heating duration. Compared to PtCo alloy and Pt nanoparticles, the $L1_n$ PtCo@Pt core-shell iNPs exhibited the strongest strain effect, benefiting from the intermetallic PtCo core and the Pt skin shell. This structure led to a 3.5% enhancement in Pt-related strain effect, outperforming the PtCo alloy, which showed a 1.56% improvement over pure Pt nanozymes. We then evaluated the POD-like performance of the $L1_0$ PtCo@Pt core-shell nanozymes on a 96-well microwell stripe plate (Fig. 1b). Notably, with increasing Pt-skin on the PtCo, the POD-like activity and specificity also increased. The $L1_0$ PtCo@Pt core-shell, possessing the strongest strain effect, demonstrated excellent POD-like activity and specificity (Fig. 1c). The inset image in Fig. 1c is a high-resolution transmission electron microscope (HRTEM) image of the $L1_0$ PtCo@Pt core-shell nanozymes, clearly indicating the Pt and Co atoms. The thermogravimetric analysis (TGA) of $L1_0$ PtCo@Pt core-shell carbon black, as shown in Fig. S1 (Supporting information), indicates that the PtCo content in the carbon black is approximately 50% by weight, as evidenced by the remaining mass after thermal decomposition. This analysis is crucial for confirming the composition and thermal stability of our synthesized material.

The nanozyme structure was characterized using transmission electron microscopy (TEM) and energy-dispersive X-ray spectroscopy (EDS). The synthesized $L1_0$ PtCo@Pt core-shell iNPs exhibited a uniform average size of 3.3 nm, featuring a distinct Pt shell, as shown in the high-angle annular dark-field (HAADF-STEM) image (Figs. 2a and b). The corresponding EDS mappings revealed that Pt and Co elements were uniformly distributed within the $L1_0$ PtCo@Pt core-shell iNPs (Fig. 2c), with EDS distinctly confirming the presence of a Pt shell. The HAADF-STEM images in Fig. S2 (Supporting information) further prove the core-shell structure of PtCo@Pt, with a Pt shell encompassing the whole particle. Furthermore, the lattice spacings of 0.36 and 0.198 nm can be respectively assigned to the (001) crystal planes of the $L1_0$ PtCo intermetallic core and the Pt shell (Fig. 2d), indicating the formation of the $L1_0$ PtCo intermetallic core and Pt shell structure. This is further corroborated by the analysis in Fig. 2e, where the Fourier transform of the (001) *d*-spacing of the $L1_0$ PtCo@Pt core-shell structure reveals distinct lattice differences. Specifically, the $L1_0$ PtCo core exhibits an average *d*-spacing of 0.36 nm, while the Pt shell shows an average *d*-spacing of 0.198 nm. These differences align consistently with HRTEM results, confirming that the core and shell possess distinct crystal structures—namely, the $L1_0$ phase for the PtCo core and the face-centered cubic (FCC) structure for the Pt shell. Additionally,

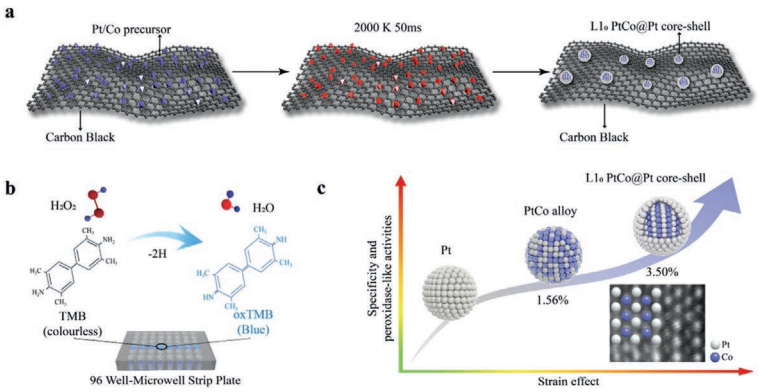


Fig. 1. (a) Schematic illustration of the Joule-heating and transient formation of PtCo core-shell structure iNPs. The diagram sequentially shows the PtCo precursor loaded on carbon black, subjected to instantaneous high-temperature heating, and the subsequent formation of $L1_0$ PtCo@Pt core-shell iNPs on carbon black. (b) Schematic representation of the peroxidase-catalyzed 3,3′,5,5′-tetramethylbenzidine (TMB) color reaction on a 96-well microwell strip plate. (c) Comparison of POD-like activity and specific properties of PtCo structures across three different configurations: PtCo intermetallic core with Pt shell, PtCo alloy, and Pt, along with a schematic diagram of their atomic arrangements.

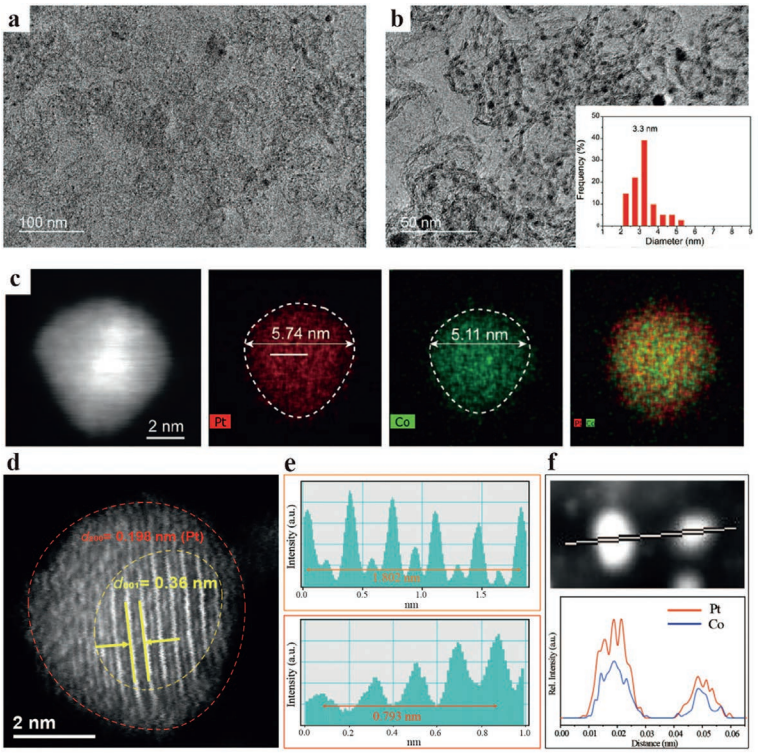


Fig. 2. (a, b) Structural characterization and particle size distribution of $L1_0$ PtCo@Pt core-shell iNPs. (c) HAADF-STEM image of $L1_0$ PtCo@Pt core-shell iNPs and its corresponding EDS elemental distribution map. (d) High-resolution image of $L1_0$ PtCo@Pt core-shell labeled with Pt shell spacing (0.18 nm) and PtCo core spacing (3.36 nm). (e) Fourier transform of the (001) *d*-spacing of $L1_0$ PtCo core and the (001) *d*-spacing of Pt shell. (f) HRTEM images of $L1_0$ PtCo@Pt core-shell iNPs and STEM-EDS line-scan analysis of an individual hybrid nanocrystal.

EDS line-scanning analyses of an $L1_0$ PtCo@Pt core-shell nanocrystal also indicated that Pt shell signals are detected across the entire $L1_0$ PtCo@Pt core-shell iNP, whereas Pt and Co signals are present across the $L1_0$ PtCo core (Fig. 2f and Fig. S3 in Supporting information).

The crystal structure of the iNPs was further confirmed by X-ray diffraction (XRD) analysis (Fig. 3a). The XRD pattern of $L1_0$ PtCo@Pt closely matched the standard peaks of PtCo intermetallic (PDF #04–001–0115), with characteristic diffraction peaks observed at 24.1° and 33.2°, corresponding to the (001) and (110) crystal planes, respectively. To further investigate the electronic structure and surface composition, X-ray photoelectron spectroscopy (XPS) was employed. As depicted in Fig. 3b, the high-resolution Pt 4f orbital could be resolved into two pairs of peaks, corresponding to Pt^0 and Pt^{2+} species, indicating that Pt in the nanozymes was primarily in its metallic state. The Pt 4f orbitals in both $L1_0$ PtCo@Pt and PtCo exhibited a negative binding energy shift compared to Pt nanozymes, confirming electron transfer from Co atoms to Pt atoms. $L1_0$ PtCo@Pt shell nanozymes were used as a POD mimic, and their enzyme-like activity was evaluated using the TMB colorimetric method. As shown in Fig. 3c, in the presence of H_2O_2, POD-like nanozymes oxidized colorless TMB to blue oxidized 3,3′,5,5′-tetramethylbenzidine (oxTMB), as following the reaction equation [41–45]:

$$H_2O_2 + H^+ \xrightarrow{POD} OH + H_2O \quad (1)$$

$$TMB + H^+ + \cdot OH \xrightarrow{POD} oxTMB + H_2O \quad (2)$$

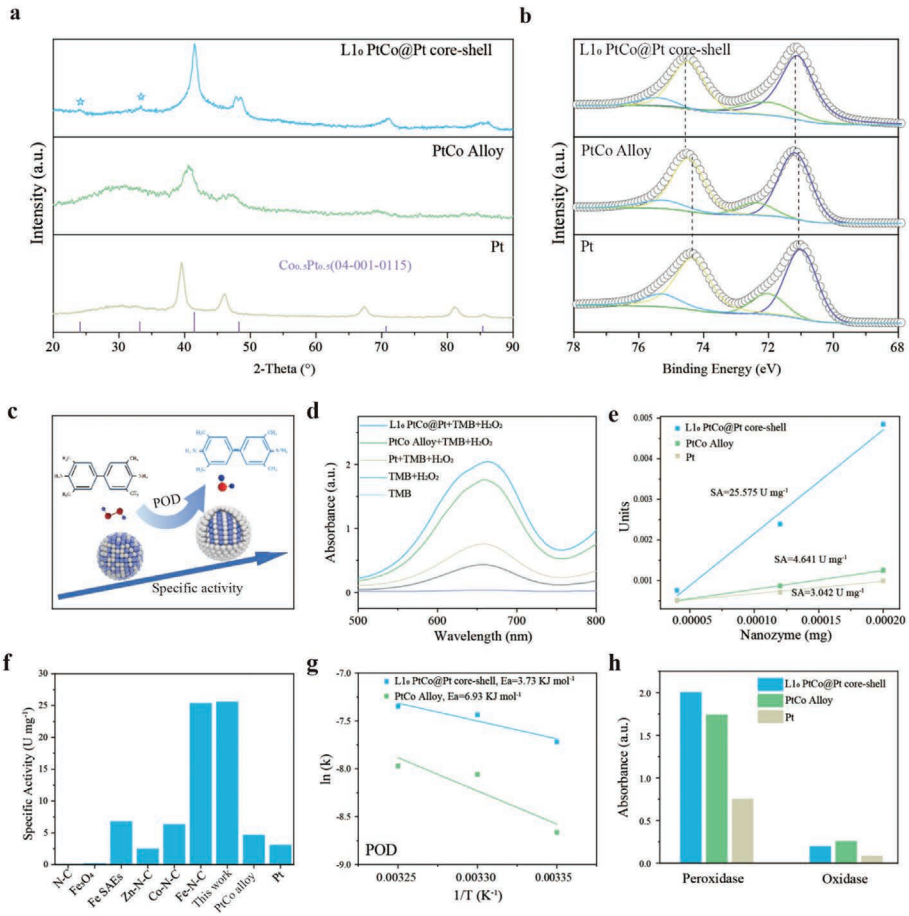


Fig. 3. (a) XRD patterns of $L1_0$ PtCo@Pt core-shell, PtCo alloy, and Pt nanozymes. (b) High-resolution XPS spectra of Pt 4f for the three nanozymes. (c) Schematic diagram of the POD-like activity reaction and specific activity size of the nanozymes. (d) Absorbance values of the H_2O_2-TMB system catalyzed by different nanozymes under identical conditions. (e) SAs of $L1_0$ PtCo@Pt core-shell, PtCo alloy, and Pt nanozymes. (f) Comparison of SA values among different nanozymes. (g) Arrhenius plots of ln(k) *versus* 1/T for POD-like activity of $L1_0$ PtCo@Pt core-shell and PtCo alloy nanozymes. (h) Comparison of POD-like and OXD-like activities of the three nanozymes.

As a control, minimal to no color change was observed in the TMB-H_2O_2 system without the nanozymes, signifying the catalytic role of the $L1_0$ PtCo@Pt core-shell nanozymes in the color change reaction. As illustrated in Fig. 3d, under identical conditions, the $L1_0$ PtCo@Pt core-shell nanozymes exhibited the highest absorbance at 652 nm, indicating their superior POD-like activity. Specific activity (SA) was employed to quantitatively assess the POD-like activity of nanozymes. As shown in Fig. 3e, the $L1_0$ PtCo@Pt core-shell nanozymes demonstrated the highest SA (25.575 U/mg), significantly outperforming the PtCo alloy (4.641 U/mg) and Pt nanozymes (3.042 U/mg). This exceptional performance places the $L1_0$ PtCo@Pt core-shell nanozyme ahead of previously reported examples [46,47], highlighting its superior efficiency and promising potential for mimicking POD-like activity (Fig. 3f).

Additionally, activation energy (E_a) for each enzyme-like activity was derived from the Arrhenius plots to elucidate the underlying mechanisms. E_a, which reflects the minimum energy required to transition from reactant to activated state, is intrinsically linked to the reaction rate. Fig. 3g illustrates that the $L1_0$ PtCo@Pt core-shell nanozymes exhibit a lower E_a value for POD-like activity (3.73 kJ/mol) compared to PtCo alloy (6.93 kJ/mol), signifying enhanced efficiency in mimicking POD activity. Specificity is also crucial for practical applications. To address this, the OXD-like activity of the nanozymes was assessed, as it could potentially introduce variability in the colorimetric detection of their POD-like activity. Fig. 3h reveals that while all three nanozymes-$L1_0$ PtCo@Pt core-shell, PtCo alloy, and Pt—demonstrate strong POD absorbance, the $L1_0$ PtCo@Pt core-shell nanozymes achieve the highest absorbance. Conversely, the OXD-like activity of all three nanozymes is negligible, underscoring the exceptional specificity of $L1_0$ PtCo@Pt core-shell nanozymes for POD-like activity.

Additionally, we evaluated the E_a for the OXD-like activity of the three nanozymes (Fig. S4a in Supporting information). The PtCo alloy exhibited a positive E_a value for OXD-like activity (0.278 kJ/mol), whereas the $L1_0$ PtCo@Pt core-shell showed a negative E_a value (−7.47 kJ/mol). This indicates that both $L1_0$ PtCo@Pt core-shell and PtCo alloy display negligible OXD-like activity compared to Pt. The enzymatic performance of the $L1_0$ PtCo@Pt core-shell nanozymes was assessed through steady-state kinetics, and the Michaelis-Menten parameters, including the Michaelis constant (K_m), the initial reaction velocity (v) and maximum reaction velocity (V_{max}), were determined using the following equation [48,49]:

$$v=\frac{V_{max}[S]}{K_m+[S]} \tag{3}$$

$$\frac{1}{v}=\frac{K_m}{V_{max}[S]}+\frac{1}{V_{max}} \tag{4}$$

In dynamic assays, the POD-like activity of the three nanozymes conformed to the Michaelis-Menten model. The enzymatic kinetic parameters, including V_{max} and K_m, are summarized in the accompanying Table S1 (Supporting information). Absorbance-time curves for $L1_0$ PtCo@Pt core-shell nanozymes were measured at various concentrations of H_2O_2 and TMB, revealing K_m values of 84.17 mmol/L for H_2O_2 (Fig. S4b in Supporting information) and

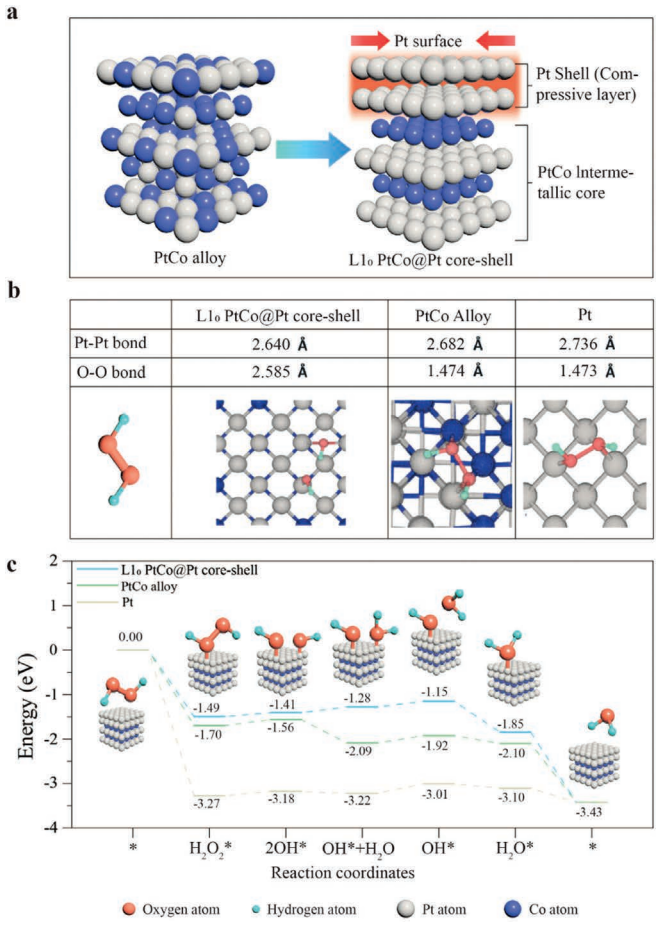


Fig. 4. (a) Schematic representation of the PtCo alloy and $L1_0$ PtCo@Pt core-shell structure. (b) Comparison of Pt-Pt and O–O bond lengths for $L1_0$ PtCo@Pt core-shell, PtCo alloy, and Pt. (c) Energy changes for $L1_0$ PtCo@Pt core-shell, PtCo alloy, and Pt at different reaction coordinates. The x-axis represents various reactants and products, while the y-axis indicates energy (eV). Different colored curves illustrate the energy changes for the three materials, with O, H, Pt, and Co atoms depicted in orange, blue, grey, and dark blue, respectively.

0.81 mmol/L for TMB (Fig. S4c in Supporting information), with corresponding V_{max} values of 2.78×10^{-7} and 2.8×10^{-7} mol L^{-1} s^{-1}, respectively. $L1_0$ PtCo@Pt core-shell nanozymes demonstrated superior Vmax values for both H_2O_2 and TMB compared to PtCo alloy and Pt, indicating their enhanced catalytic activity. Additionally, the significantly lower K_m values for $L1_0$ PtCo@Pt core-shell nanozymes suggest a higher affinity for the catalytic substrates. These findings underscore the exceptional catalytic performance of $L1_0$ PtCo@Pt core-shell nanozymes in H_2O_2 decomposition.

The remarkable enhancement in activity observed for $L1_0$ PtCo@Pt core-shell nanozymes is likely attributed to two key strain-induced effects: (1) The selective incorporation of Co atoms into specific lattice sites within Pt, which amplifies the strain effects [27,50]; and (2) the exposure of Pt [001] crystal facets, which exhibit well-defined anisotropic strains [26,51]. These factors collectively facilitate accelerated electron transfer during the catalytic reaction, significantly boosting the POD-like activity of the PtCo@Pt core-shell nanozymes.

To elucidate the mechanism behind the enhanced activity of POD nanozyme catalysts, we conducted first-principles density functional theory (DFT) calculations on $L1_0$ PtCo@Pt core-shell nanozymes, PtCo alloy nanozymes, and Pt nanozymes. We constructed a core-shell structure model of PtCo with a metal atom ratio of 1.5:1. The models, as shown in Fig. 4a, feature PtCo atoms interspersed in the (110) plane with a Pt atomic shell coating the outer surface, representing the core-shell configuration. For comparison, a PtCo alloy model was also constructed as a direct confirmation of the compression/tension effects on the Pt surface plane. When Co atoms with relatively small lattice parameters are inserted into the Pt lattice, due to the difference in lattice parameters between the two, a lattice mismatch phenomenon occurs, thereby generating a strain effect. This strain effect can cause the lattice spacing to contract, shortening the Pt−Pt bond length. The contraction of the lattice will lead to the shift of the d-band center to a higher energy direction, and this change is beneficial for enhancing the adsorption of reaction intermediates on the catalyst surface. To experimentally verify the impact of these structural changes, the distances between adjacent Pt sites on the surfaces of pure Pt, PtCo alloy, and $L1_0$ PtCo@Pt core-shell structures were measured, marked with grey balls, and found to be 2.64, 2.682, and 2.736 Å, respectively (Fig. 4b). Comparing these distances, it was observed that the Pt surface lattice parameter of $L1_0$ PtCo@Pt core-shell was compressed by 3.50 % relative to that of pure Pt. This indicates that the core structure with a Pt shell creates a stress environment, subjecting the Pt surface plane on the $L1_0$ PtCo intermetallic to a certain degree of compression. Moreover, the high symmetry of the $L1_0$ PtCo intermetallic core ensures controllable and long-range ordered lattice parameters, allowing uniform modulation of surface compressive stress. By covering the surface with a Pt layer, PtCo alloys form a core-shell structure in which the Pt shell acts as a compression layer, inducing a strain effect on the surface layer of Pt, potentially enhancing POD-like catalytic performance.

To elucidate the superior POD-like performance of $L1_0$ PtCo@Pt core-shell nanozymes, we provide the atomic model of the H_2O_2 reaction site in Fig. 4b. The O–O bond lengths of H_2O_2 adsorbed on the surfaces of $L1_0$ PtCo@Pt core-shell, PtCo alloy, and Pt were measured at 2.585, 1.474, and 1.473 Å, respectively. The $L1_0$ PtCo@Pt core-shell displays the longest O–O bond, while the bond lengths for PtCo alloy and Pt are similar and shorter. Longer O–O bonds facilitate easier molecular dissociation. Furthermore, we calculated the POD-like evolution process. Initially, the nanozyme adsorbs activated H_2O_2, which then undergoes pyrolysis to form two adsorbed hydroxyl groups (OH^*), followed by gradual protonation to form H_2O^* and subsequent desorption. The calculated energy changes for these steps are summarized in Fig. 4c, showing that the thermodynamic energy decreases for the splitting of $H_2O_2^*$ across all three models. The energy change for this step is lowest for $L1_0$ PtCo@Pt core-shell, followed by PtCo alloy and Pt. Among the various steps in the reaction process, the rate-determining step (RDS) for the $L1_0$ PtCo@Pt core-shell structure occurs at the third step (from $H_2O^* + OH^*$ to OH^*), whereas for PtCo alloy and Pt, it is at the fourth step (from OH^* to H_2O^*). Notably, the $L1_0$ PtCo@Pt core-shell structure demonstrates a significantly lower RDS energy barrier (0.128 eV) compared to the PtCo alloy (0.211 eV) and Pt (0.1664 eV), highlighting its superior catalytic kinetic performance. This lower RDS barrier explains the superior POD-like activity of $L1_0$ PtCo@Pt core-shell nanozymes, which is induced by the strain effects from the PtCo intermetallic core and Pt shell. These effects stem from the selective incorporation of Co atoms into specific lattice sites within Pt, which intensifies the strain effects. On the other hand, the exposure of Pt (001) crystal facets is characterized by well-defined anisotropic strains. Together, these factors promote faster electron transfer during the catalytic reaction, significantly enhancing the POD-like activity of the $L1_0$ PtCo@Pt core-shell nanozymes.

In summary, our study reveals the significant potential of $L1_0$ PtCo@Pt core-shell iNPs, which exhibit exceptional POD-like activity and specificity due to strain-induced effects at the Pt skin and PtCo core interface. The synthesized $L1_0$ PtCo@Pt core-shell nanozymes demonstrate SA of 25.545 U/mg, a remarkable 17.4-fold increase compared to Pt nanoparticles, and exhibit mini-

mal OXD-like activities. Theoretical calculations and experimental data corroborate that the core-shell structure effectively lowers both the adsorption energy of H_2O_2 and the activation energy for the rate-determining step. Furthermore, the Supporting Information demonstrates that the capability of these nanozymes for accurate colorimetric detection of carcinoembryonic antigen underscores their practical utility. Looking forward, the $L1_0$ PtCo@Pt core-shell nanozymes present a promising and versatile platform for future advancements, offering substantial potential for applications in biomedical diagnostics, environmental sensing, and other fields requiring high catalytic efficiency and specificity.

Declaration of competing interest

The authors declare no conflict of interest.

CRediT authorship contribution statement

Bo Xu: Writing – original draft, Investigation. **Mingjin Cui:** Writing – review & editing, Writing – original draft, Supervision, Data curation, Conceptualization. **Zhimin Luo:** Writing – review & editing, Conceptualization. **Lianhui Wang:** Validation, Supervision.

Acknowledgments

M. Cui acknowledges the support from the Natural Science Foundation for Young Scholars of Jiangsu Province (No. BK20230371); National Natural Science Foundation of China (No. 52403308); Natural Science Foundation of Shanghai (No. 24ZR1452600); The Postgraduate Research & Practice Innovation Program of Jiangsu Province (No. 46030CX23982).

Supplementary materials

Supplementary material associated with this article can be found, in the online version, at doi:10.1016/j.cclet.2025.111227.

References

[1] D. Jiang, D. Ni, Z.T. Rosenkrans, et al., Chem. Soc. Rev. 48 (2019) 3683–3704.
[2] M. Liang, X. Yan, Acc. Chem. Res. 52 (2019) 2190–2200.
[3] Y. Lin, J. Ren, X. Qu, Acc. Chem. Res. 47 (2014) 1097–1105.
[4] H. Wei, E. Wang, Chem. Soc. Rev. 42 (2013) 6060–6093.
[5] J. Wu, X. Wang, Q. Wang, et al., Chem. Soc. Rev. 48 (2019) 1004–1076.
[6] M. Zandieh, J. Liu, Adv. Mater. 36 (2024) 2211041.
[7] J. Feng, X. Yang, T. Du, et al., Adv. Sci. 10 (2023) 2303078.
[8] G. Jiang, Q. Xu, J. Xie, et al., Adv. Funct. Mater. 34 (2024) 2405190.
[9] L. Li, L. Cao, X. Xiang, et al., Adv. Funct. Mater. 32 (2022) 2107530.
[10] W. Yang, X. Yang, L. Zhu, et al., Coord. Chem. Rev. 448 (2021) 214170.
[11] X. Zhang, S. Lin, S. Liu, et al., Coord. Chem. Rev. 429 (2021) 213652.
[12] J. Mujtaba, J. Liu, K.K. Dey, et al., Adv. Mater. 33 (2021) 2007465.
[13] Z. Yang, J. Guo, L. Wang, et al., Small 20 (2024) 2307815.
[14] J. Chen, X. Liu, G. Zheng, et al., Small 19 (2023) 2205924.
[15] J. Chen, Q. Ma, M. Li, et al., Nat. Commun. 12 (2021) 3375.
[16] J. Huang, L. Jiao, W. Xu, et al., ACS Appl. Mater. Interfaces 13 (2021) 33383–33391.
[17] X. Liu, X. Liang, J. Yu, et al., Trends Anal. Chem. 169 (2023) 117386.
[18] D. Wang, J. Wang, X.J. Gao, et al., Adv. Mater. 36 (2024) 2310033.
[19] M. Feng, X. Li, X. Zhang, Y. Huang, Trends Anal. Chem. 166 (2023) 117220.
[20] R. Fu, Z. Ma, H. Zhao, et al., Anal. Chem. 95 (2023) 10844–10858.
[21] F. Meng, P. Zhu, L. Yang, et al., Chem. Eng. J. 452 (2023) 139411.
[22] H. Sun, Y. Zhou, J. Ren, X. Qu, Angew. Chem. Int. Ed. 57 (2018) 9224–9237.
[23] J. Li, L. Luo, S. Wang, et al., PhotoMat 1 (2024) 1–14.
[24] H. Guo, S. Guo, CCS Chem. 7 (2024) 326–344.
[25] C. Liu, L. Gui, J.J. Zheng, et al., J. Am. Chem. Soc. 145 (2023) 19086–19097.
[26] Z. Wang, R. Zhang, X. Yan, K. Fan, Mater. Today 41 (2020) 81–119.
[27] J. Wu, Q. Liu, D. Jiao, et al., Angew. Chem. Int. Ed. 63 (2024) e202403203.
[28] Z. Xi, X. Cheng, Z. Gao, et al., Nano Lett. 20 (2019) 272–277.
[29] J. Zhang, Y. Chen, M.G. Li, et al., Nano Lett. 24 (2024) 14373–14380.
[30] Y. Ai, M.Q. He, H. Sun, et al., Adv. Mater. 35 (2023) 2302335.
[31] Y. Nie, Z. Li, Y. Wang, et al., Appl. Catal. B 343 (2024) 123494.
[32] Y. Tang, Y. Chen, Y. Wu, et al., Nano Lett. 23 (2022) 267–275.
[33] W. Xie, G. Zhang, Z. Guo, et al., Mater. Today Bio 16 (2022) 100411.
[34] X. Yang, M. Tan, J. Guo, et al., Adv. Funct. Mater. 34 (2024) 2401963.
[35] L. Zhu, Z. Lai, J. Xu, et al., J. Mater. Chem. A 12 (2024) 28149–28160.
[36] W. Yang, L. Shang, X. Liu, et al., Chin. Chem. Lett. 35 (2024) 109501.
[37] M. Cui, C. Yang, S. Hwang, et al., Nano Lett. 22 (2022) 255–262.
[38] Z. Huang, T. Li, B. Li, et al., J. Am. Chem. Soc. 146 (2024) 2167–2173.
[39] B. Deng, L. Eddy, K.M. Wyss, et al., Nat. Rev. Clean Technol. 1 (2025) 32–54.
[40] M. Winter, WebElements Periodic Table, University of Sheffield, 2025.
[41] X. Liu, J. Yang, J. Cheng, et al., Sens. Actuator. B 337 (2021) 129763.
[42] Y. Xu, A. Huang, W. Yi, et al., Coord. Chem. Rev. 500 (2024) 215517.
[43] L. Yang, X. Xu, Y. Song, et al., Chem. Eng. J. 487 (2024) 150612.
[44] X. Yu, Y. Wang, J. Zhang, et al., Adv. Healthcare Mater. 13 (2024) 2302023.
[45] H. Zhu, J. Deng, S. Mu, et al., Chem. Eng. J. 462 (2023) 142215.
[46] L. Jiao, J. Wu, H. Zhong, et al., ACS Catal. 10 (2020) 6422–6429.
[47] C. Zhao, C. Xiong, X. Liu, et al., Chem. Commun. 55 (2019) 2285–2288.
[48] B. Jiang, D. Duan, L. Gao, et al., Nat. Protoc. 13 (2018) 1506–1520.
[49] X. Shen, Z. Wang, X.J. Gao, X. Gao, Adv. Mater. 36 (2024) 2211151.
[50] S. Zhong, Z. Zhang, Q. Zhao, et al., Nat. Commun. 15 (2024) 8097.
[51] X. Yu, L. Wang, Z. Zhu, et al., Small 19 (2023) 2304818.